Stretchable Thermoelectric Generators for Self-Powered Wearable Health Monitoring

Mason Zadan, Anthony Wertz, Dylan Shah, Dinesh K. Patel, Wuzhou Zu, Youngshang Han, Jeff Gelorme, Hing Jii Mea, Lining Yao, Mohammad H. Malakooti, Seung Hwan Ko, Navid Kazem, and Carmel Majidi*

As continuous wearable physiological monitoring systems become more ubiquitous in healthcare, there is an increasing need for power sources that can sustainably power wireless sensors and electronics for long durations. Wearable energy harvesting with thermoelectric generators (TEGs), in which body heat is converted to electrical energy, presents a promising way to prolong wireless operation and address battery life concerns. In this work, high performance TEGs are introduced that combine 3D printed elastomers with liquid metal epoxy polymer composites and thermoelectric semiconductors to achieve elastic compliance and mechanical compatibility with the body. The thermoelectric properties are characterized in both energy harvesting (Seebeck) and active heating/cooling (Peltier) modes, and examine the performance of wearable energy harvesting under various conditions such as sitting, walking, and running. When worn on a user's forearm while walking outside, the TEG arrays are able to power circuitry to collect photoplethysmography (PPG) waveform data with a photonic sensor and wirelessly transmit the data to an external PC using an on-board Bluetooth Low Energy (BLE) radio. This represents a significant step forward on the path to sustainable body-worn smart electronics.

1. Introduction

Portable, wearable electronics for physiological monitoring, in contrast to their tethered counterparts in clinical settings, increasingly require larger power sources to support greater computational, sensing, and communication demands over long durations of continuous or frequent monitoring. Potential routes to address this problem include incorporating large batteries or requiring frequent recharging, which may become impractical for long-term monitoring, especially for devices that are difficult to reach, remove, or reapply. An alternative route is to incorporate on-body energy harvesting to extend durations between battery recharging cycles and potentially eliminate the need for a battery all together. Such an approach requires wearable generators that are highly miniaturized or sufficiently soft and flexible to be worn on the body without interfering with natural motion. Recent research has developed methods for harvesting biomechanical energy through piezoelectric, triboelectric, and dieletric energy conversion methods, along with body heat through thermoelectric energy conversion.[1–5] Thermoelectric devices (TEDs)[6,7] are especially promising due to their ability to harvest energy under a wide range of conditions, including for indoor, outdoor, active, and sedentary activities. Thermoelectric devices operate on two main principles, the Seebeck and Peltier effects. In the Seebeck effect, a thermal

M. Zadan, D. K. Patel, W. Zu, C. Majidi
Department of Mechanical Engineering
Carnegie Mellon University
5000 Forbes Ave, Pittsburgh, PA 15213, USA
E-mail: cmajidi@andrew.cmu.edu

A. Wertz, C. Majidi
Robotics Institute
Carnegie Mellon University
5000 Forbes Ave, Pittsburgh, PA 15213, USA

D. Shah, J. Gelorme, H. J. Mea, N. Kazem
Arieca Inc.
201 N Braddock Ave Suite 334, Pittsburgh, PA 15208, USA

D. K. Patel, L. Yao
Human Computer Interaction Institute
Carnegie Mellon University
5000 Forbes Ave, Pittsburgh, PA 15213, USA

Y. Han, M. H. Malakooti
Department of Mechanical Engineering
University of Washington
3900 E Stevens Way NE, Seattle, WA 98195, USA

S. H. Ko
Department of Mechanical Engineering
Seoul National University
1 Gwanak-ro, Gwanak-gu, Seoul 08826, South Korea

**ADVANCED
SCIENCE NEWS**

www.advancedsciencenews.com

**ADVANCED
FUNCTIONAL
MATERIALS**

www.afm-journal.de

gradient is applied across the semiconductor junctions of two oppositely doped semiconductors, inducing a current which can be used for energy harvesting. Conversely, the Peltier effect occurs when a voltage is applied across the semiconductor junctions inducing a temperature differential and enabling solid-state cooling.[8] However, for TEDs to be seamlessly integrated into wearables, they must be elastically compliant in order to conform to the body, moderately stretchable so that they do not interfere with the user's natural mechanics, and sufficiently soft so that they can mechanically interface with the skin without introducing air gaps or stress concentrations that could result in high thermal resistance or skin discomfort.[9–14] To accomplish this, progress depends on a new class of soft high-performance materials to match or exceed the energy harvesting performance of rigid TEDs while presenting minimal mechanical resistance to elastic deformation to ensure comfort and effective heat transfer.[1]

Recent TEG research has focused on improving interconnects and thermal interface materials (TIM) to improve device performance. To replace traditional rigid copper interconnects, flexible and wavy copper sheets,[10,11,15–17] liquid metals (LM),[12,14,18] and LM-based composite materials[19] have been introduced. Methods based on rigid metals such as copper are highly promising, but potentially suffer from limitations due to their intrinsic mechanical stiffness, which can lead to localized stress concentrations and may require complex manufacturing methods and geometries to achieve effective mechanical compliance at the meso/macroscale.[20,21] Likewise, microfluidic channels of LM alloys, such as eutectic gallium indium (EGaIn) embedded within a soft elastomer, allow for improved mechanical performance but can be prone to leaking and subsequent electrical short-circuiting during fabrication, lowering the potential for high semiconductor packing densities.[14] To overcome these limitations, a promising alternative is to use percolating networks of LM droplets embedded within a soft elastomer. In contrast to microfluidic channels of bulk liquid metal, these LM-embedded elastomer (LMEE) composites support high electrical conductivity that remains stable under extreme strain and are less prone to leakage due to the robust encapsulation of LM droplets within the surrounding polymer.[22,23] Moreover, LMEEs can also be engineered to be electrically insulating and function as a high-performance TIM, to decrease the thermal resistance between the semiconductors within the TED and interfaces to the body and surrounding environment. LMEEs have previously been implemented as a TIM and heat sink for TEDs,[24–27,53] although researchers have also explored other materials for thermal management including radiative absorbing materials,[28] flexible phase change materials,[29] graphene nanoplatelets,[30] Ag–Ni aligned networks,[31] Ag and CNT-embedded elastomers,[11] and fin based soft heat sinks.[19,26,32] Nonetheless, in spite of such advancements, the thermal conductivities of TIMs used in TEDs have been reported to be at most ≈ 1.1 Wm^{-1} K^{-1}, therefore representing another potential area for improvement.

Building on these material architectures, there have been several attempts in recent years to incorporate TEDs into wearable electronics to power health monitoring sensors. However, these demonstrations have largely focused on small-scale low-power implementations. Examples include implementations that perform temperature and humidity measurements,[33] ECG measurements,[17,34] a three-axis accelerometer,[35] gyroscope measurements, and Bluetooth transmission.[36] However, there still remains to be demonstrated a mechanically soft and wearable TEG that can power a more energy-intensive physiological sensing capability like photoplethysmography (PPG), which is used to capture health vitals like heart rate and SpO$_2$ blood oxygenation. Achieving photonic sensing in a battery-free wearable device that is also capable of energy storage, signal processing, and wireless transmission remains a key remaining challenge in the field.[2]

In this work, we address this critical need by introducing a new framework to design battery-free wearable electronics that are capable of photonic-based physiological monitoring and fully powered using body heat. Each element of the system design has been selected to achieve high mechanical and thermoelectric performance, along with seamless materials integration. This is accomplished through a comprehensive design and manufacturing framework that includes advancements in soft-matter material architectures, TEG array design, low energy circuit board design, and on-board power management (**Figure 1**). The devices comprise a high-aspect-ratio 3D printed elastomer matrix for mechanical compliance and high semiconductor fill factor, an elastomeric LM-epoxy composite for enhanced thermal conductivity between the TED and contacting surfaces, and an LM-Ag-SIS elastomer ink composite for mechanically robust electrical connectivity between bismuth telluride (Bi_2Te_3) thermoelectric semiconductor elements. Compared to past work with LM-based soft TEG architectures, this approach allows for greater freedom in semiconductor densities and aspect ratio of the semiconductors. Moreover, it incorporates a stretchable LM-epoxy composite with the highest recorded thermal conductivity (2.90 ± 0.02 Wm^{-1} K^{-1}) of any TIM used for a wearable TEG. A variety of soft TEGs were implemented using this general design framework and compared across their Seebeck, Peltier, and electromechanical properties. In particular, Seebeck, Peltier, and electromechanical performance were compared for semiconductor densities of 40 % versus 22 %, the incorporation of the stretchable LM-epoxy composite vs a non-thermally conductive epoxy, and the use of high-aspect ratio semiconductors (4:1.4) versus low-aspect ratio semiconductors (1.6:1.4) for heat transfer performance. This novel device framework, enabled by the material architectures introduced herein, produces TEGs that achieve the goal of combining mechanical compliance and elasticity (30 % uniaxial strain), high semiconductor fill densities (40 % fill factor), and high power outputs of 4.95 mW, (0.40 mWcm^{-2}) at 20 °C and 35.85 mW (3.32 mWcm^{-2}) at 60 °C (Video S1, Supporting Information).

While bench-top characterization can give accurate performance metrics, operation on the body introduces a host of parameters that must be understood in order for TEGs to be integrated with wearable sensors. There is still a gap in the literature on characterizing energy harvesting performance on the body.[10,37,38] To address this, we conducted comprehensive on-body characterization, analyzing the influence of TEG body placement and the influence of exertion and bio-mechanical movement on Seebeck output. Voltage output, heart rate, and surface and skin temperature are recorded during sitting, walking, and run tests mounted to the chest and forearm. The insights gained here are instrumental in designing a fully self-powered vitals
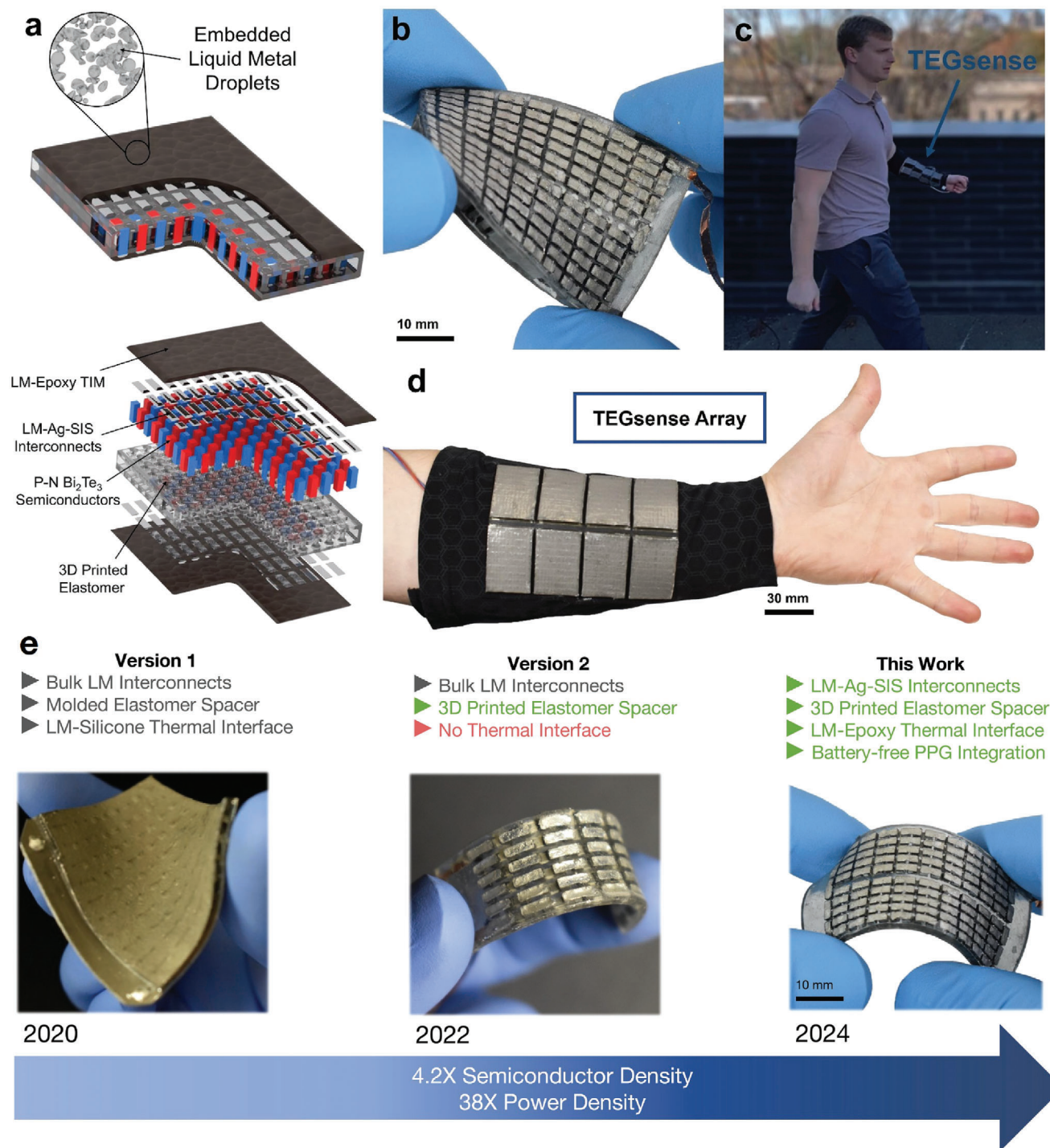
**ADVANCED
SCIENCE NEWS**

www.advancedsciencenews.com

**ADVANCED
FUNCTIONAL
MATERIALS**

www.afm-journal.de

Figure 1. Design and overview of wearable thermoelectric device. a) TEG Schematic showing the key components of soft thermal interface materials, LM-Ag-SIS stretchable conductive inks, Bi_2Te_3 semiconductors, and 3D printed elastomer matrix. b) Image of TEG in flexure highlighting high semiconductor density of LM-Ag-SIS inks. c) Image of TEGsense PPG monitoring wearable being worn on the arm during operation. d) Image of TEGsense array made from eight HA-HD + LM-epoxy TEGs. e) Design and performance comparison of previous stretchable TEG works. Reproduced with permission.[24] Copyright 2020, American Chemical Society. Reproduced with permission.[13] Copyright 2022, Wiley-VCH.

monitoring wearable powered by body heat. By integrating an array of eight stretchable TEGs with custom hardware, we introduce TEGsense, the first device that demonstrates wireless and battery-free photonic PPG wearable monitoring that can harvest energy from body heat, store harvested energy, boost to operational voltage, communicate with an optical PPG board, process data, and transmit data over BLE. This forearm-worn sleeve can operate indefinitely without the need for charging or connection to a data logger as long as an adequate temperature differential exists. (Figure 1c,d). Collectively, the work presented here exhibits a new milestone for battery-free wearables, acting as a first step to fill the gap of photonic-based PPG sensing powered solely by the body, a key open target in the field.[2] This new framework for TED design generates an order-of-magnitude increase in power density over our previous designs[13,24] (Figure 1e) and builds off of the past successes of implementing large TEG arrays in aquatic environments for sensing.[39]

2. Results and Discussion

2.1. TED Design and Fabrication

The high Seebeck, Peltier, and mechanical performance of the devices introduced here were enabled through a unique combination of LM-based material architectures and material integration approaches (Figure 1a; Figure S1, Supporting Information). First, a deformable acrylate-based resin[40,41] was 3D printed using digital light processing (DLP), creating the center layer to enable complex internal structural designs to achieve mechanical deformability while maintaining a low thermal conductivity of ≈0.19 W m^{-1} K^{-1} to mitigate heat transfer. This material exhibits < 1% thermogravimetric loss at 220 °C and excellent mechanical compliance, making it appropriate for wearable energy harvesting applications (Figure S2, Supporting Information). Bi_2Te_3 semiconductors were then placed into the printed slots of the center substrate, in a p–n π configuration. A soft 3D-printed stencil of the acrylate-based material was then placed over the semiconductors, forming sealed wells for the conductive ink to fill. Next, we airbrushed a thin layer of EGaIn onto the stencil to mitigate contact resistances. The LM-Ag-SIS ink solution was used to electrically connect the semiconductors with conductivity coming from the percolating network of EGaIn droplets and Ag flakes, along with regions of alloyed AgIn. This ink was chosen due to its low electromechanical coupling, high strain limit, and high electrical conductivity.[42,43,52] The LM-Ag-SIS ink solution was injected into the wells of the stencil connecting together the LM-coated semiconductors, producing traces. The ink's processability and stability during deposition allowed for greatly improved manufacturability and decreased chance of shorting, allowing us to achieve higher semiconductor densities compared to bulk LM approaches.

Once the ink was deposited, we removed the stencil and allowed the solvent to evaporate, leaving low-resistance connected traces. To protect the circuitry, an encapsulation layer of either an LM-epoxy composite (made by shear-mixing liquid metal and epoxy resins) or UV-curable resin was deposited and cured on the top layer. By comparing the two encapsulation materials (in subsequent sections), we were able to determine the effects that improving the thermal contact resistance would have on de-

vice performance. The circuit fabrication process was then repeated on the backside. Images of the completed devices are given in **Figure 2a–d**, highlighting the various fill factors (fraction of semiconductor surface area over overall surface area), aspect ratios, and encapsulation layers compared in this work. Further fabrication details can be found in the Experimental Section.

2.2. Thermoelectric Device Performance with Varying Design Parameters

2.2.1. Semiconductor Aspect Ratio Performance Comparison

To better understand the influence of semiconductor aspect ratio on holding a temperature differential and generating a high voltage output, we compared devices with high and low aspect ratio semiconductors. Both device types had similar fill factors (42 % and 39 %) but with two different semiconductor dimensions selected: 1.4 × 1.4 × 1.6 mm and 1.4 × 1.4 × 4 mm, respectively referred to as Low-Aspect High-Density (LA-HD) (Figure 2a; Figure S3, Supporting Information) and High-Aspect High-Density designs (HA-HD) (Figure 2b; Figure S4, Supporting Information). The HA-HD had the addition of a hollow center structure with pillars to increase mechanical compliance for this taller configuration.

For evaluating the Seebeck energy harvesting performance, we measured open circuit voltage (V_{oc}) versus temperature difference (ΔT) (Figure 2e; Figure S5a, Supporting Information), along with voltage density (Figure S5b, Supporting Information). Seebeck voltage followed a linear relationship, as predicted by $V = n\alpha\Delta T$, where n is the number of thermocouples, α the difference in Seebeck coefficients between the p and n-type semiconductors, and ΔT was the temperature differential across the device. HA-HD exhibited a 40 % and 45 % increase over LA-HD at $\Delta T = 10$ and 60 °C respectively. Increasing the distance between the depletion regions and decreasing the thermal conductance between the hot and cold faces of the device leads to a slower degradation of the thermal gradient and higher voltage output (Figure S6a,b, Supporting Information).

Peltier cooling and heating improvements were also demonstrated with the use of high-aspect ratio (HAR) semiconductors (Figure 2f; Figure S7a,b, Supporting Information). At 0.75 A, cooling ΔT peaks at -4.8 ± 0.7 °C at 2.8 s for LA-HD compared to -13.0 ± 0.6 °C at 8.8 s for HA-HD. Heating performance confirms this trend, with temperature increases at 0.75 A of 49.1 ± 4.0 °C for LA-HD compared to 84.8 ± 4.0 °C at 45 s for HA-HD (see Section S2, Supporting Information).

While Seebeck and Peltier performance increased with the HAR semiconductors, mechanical performance decreased due to the increase in bending moment. After 10 cycles of 20 % compressive loads, Euler's critical load (P_{cr}) and flexural rigidity (EI) increased from $P_{cr} = 0.79$ N and 4.21×10^{-5} Nm^2 for LA-HD to $P_{cr} = 3.20$ N and 1.72×10^{-4} Nm^2 for HA-HD, with elastic and plastic regimes appearing in both curves along with relative resistance change staying under 0.05 for both devices (Figures 2g,h and 3a,b). The use of HA-HD semiconductors produced a device with much better electrical performance, but with the trade-off of increased mechanical rigidity.
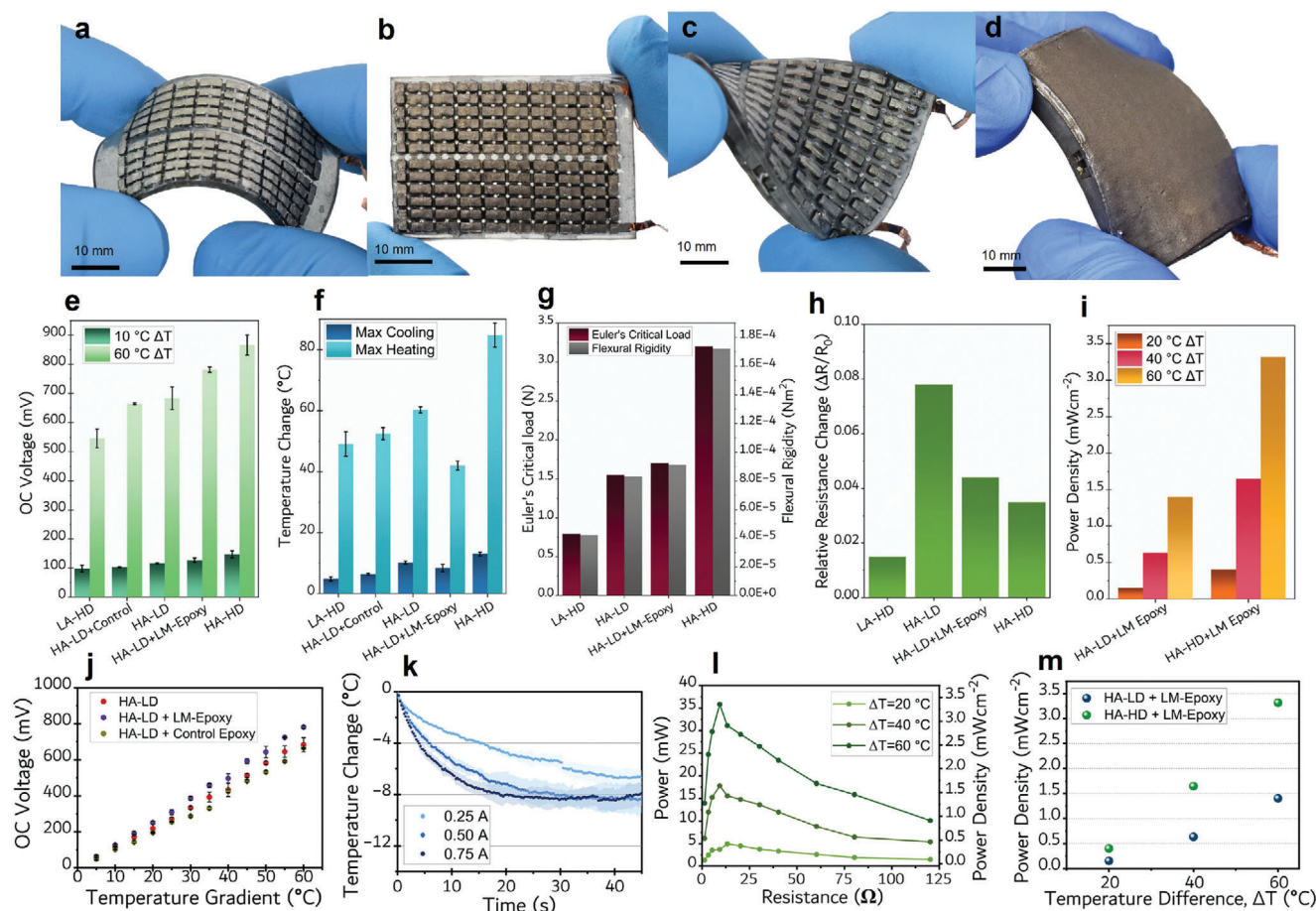
Figure 2. Characterization of TEG Configurations. Images of a) Low-Aspect High-Density (LA-HD), b) High-Aspect High-Density (HA-HD), c) High-Aspect Low-Density (HA-LD), d) and High-Aspect Low-Density+LM-epoxy TEG configuration. e) Seebeck open-circuit voltage performance at $\Delta T = 10$ °C and $\Delta T = 60$ °C for various TEG configurations. f) Peltier performance of max cooling and max heating for various TEG configurations. g) Mechanical performance of TEG configurations comparing flexural rigidity and Euler's critical load. h) Relative resistance change performance. i) Power density comparison between HA-LD + LM-epoxy and HA-HD + LM-epoxy TEG configuration at $\Delta T = 20, 40, 60$ °C. j) Open-circuit voltage versus temperature comparing HA-LD, HA-LD + LM-epoxy, and HA-LD + Control Epoxy configurations. k) Peltier cooling performance of High-Aspect Low-Density + LM-epoxy configurations. l) Power output versus external load Resistance for HA-HD + LM-epoxy TEG at $\Delta T = 20, 40, 60$ °C. m) Comparison of peak power outputs for HA-LD + LM-epoxy and HA-HD + LM-epoxy TEGs.

2.2.2. Semiconductor Fill Density Performance Comparison

Mechanical compliance is important not only from a comfort and compatibility perspective, but also to decrease the thermal resistance between the skin and device through constant contact with the body during movement. Decreasing the density of rigid semiconductors is one way to increase flexibility and potentially improve mechanical performance. A device with a lower fill density of 22 % referred to as high-aspect low-density (HA-LD) TEG was fabricated and compared (Figure 2c; Figure S8, Supporting Information) to HA-HD. HA-LD TED underperforms the HA-HD device by 24 % at both 10 and 60 °C. When normalized over the surface area, the HA-LD V_{oc} was within the margin of error of the LA-HD (Figure S5b, Supporting Information). Still, the voltage drop over time is improved over LA-HD (Figure S6c, Supporting Information).

Peltier heating and cooling performance is given in Figure S7c (Supporting Information) for HA-LD. For Peltier cooling and heating, the cooling performance (ΔT) at 0.75 A peaked at -10.2 ± 0.5 °C @ 15.3 s with heating performance of 60.3 ± 1.0 °C at 45 s, performing in between LA-HD and HA-HD devices. Mechanically, performance for 10 cycles at 20 % compression was in between LA-HD and HA-HD mechanical performance with a less defined Euler critical load of $P_{cr} = \sim 1.55$ N and flexural rigidity of 8.31×10^{-5} Nm^2 with an intra-cycle relative resistance change of ≈ 0.05 (Figure 2g,h). For operation on less curved and more stable surfaces such as the forearm for wearable energy harvesting, HA-HD is still ideal due to high Seebeck output.

2.2.3. Thermal Interface Performance Comparison

The devices characterized in previous sections of this work relied on a thin (≈ 300 μm) UV curable ink with a low thermal conductivity (≈ 0.19 Wm^{-1} K^{-1}) that was applied onto the surface
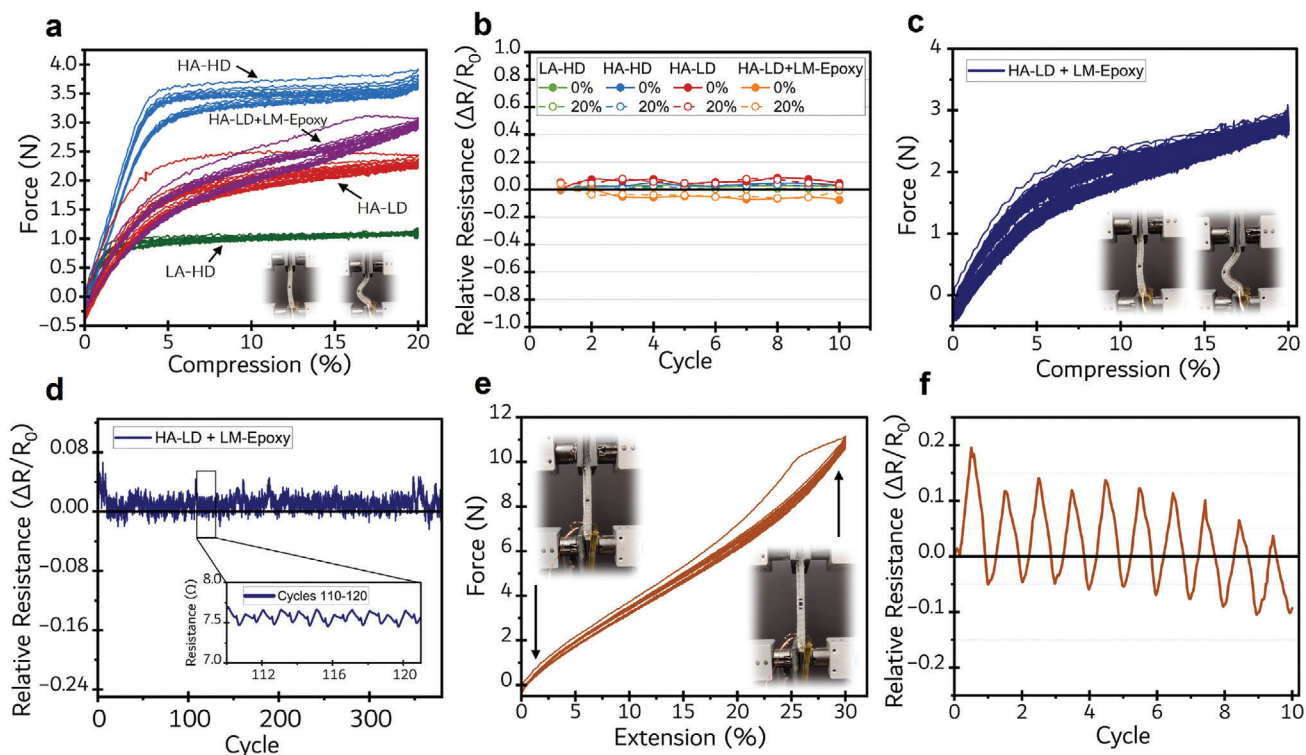
Figure 3. Electromechanical Characterization: a) Compression versus force comparison for 10 cycles at 20% compression. Inset shows a HA-LD device at 0% (left) and 20% compression (right). b) Comparison of change in relative resistance at 20% compression for 10 cycles. c) Mechanical performance at 20% compression for 380 cycles for HA-LD + LM-epoxy device. Inset: Images of device at 0% and 20% compression. d) Change in relative resistance over 380 cycles at 20% compression for HA-LD + LM-epoxy TEG. Inset: resistance at cycles 110–120. e) Mechanical performance at 30% uni-axial strain for 10 cycles for HA-LD + LM-epoxy device. Inset: Images highlighting 0% and 30% extension. f) Relative resistance change over 10 cycles at 30% extension for HA-LD + LM-epoxy TED.

(Figure S2, Supporting Information). This thin layer was prone to damage leaving interconnects exposed. To address this, we developed and utilized a custom-formulated epoxy composed of polypropylene glycol and diglycidyl ether that allows for robust adhesion to the TED without impeding mechanical compliance. In order to achieve high thermal conductivity, we added a ≈65% volume loading of EGaIn to the epoxy, and shear-mixed to attain a homogeneous suspension. EGaIn was selected as the metallic filler since it has a high thermal conductivity of $26.4\,Wm^{-1}\,K^{-1}$ while being liquid at room temperature.[44] The thermal properties of the the LM-epoxy formulation were measured using a Nanotest TIMA 5 thermal interface material analyzer. For a bondline thickness of 750 μm, we observed a thermal resistance with respect to area of $257.5 \pm 1.6\,mm^2\,KW^{-1}$ and volumetric thermal conductivity of $2.90 \pm 0.02\,Wm^{-1}\,K^{-1}$ (Figure S9a,b, Supporting Information). This represents a ≈2× improvement in thermal performance compared to previous thermally conductive elastomers that use liquid metal or other filler particles.[11,24,26,30,45,46] Additionally, this LM-epoxy bonded well to the 3D printed elastomer used as the substrate, with a work of adhesion of $5.4 \times 10^{-2}\,Jm^{-2}$ and a peel force of 1.15 N. (Figure S9c, Supporting Information). This material was developed to improve the lifetime of the devices, by protecting the interconnects from damage, along with improving heat transfer and voltage output.

An HA-LD version with LM-epoxy composite (Figure 2d; Figure S10, Supporting Information) was fabricated along with control samples with an unfilled epoxy, to compare the influence of using a TIM to coat the two sides of the TED (Figure S11, Supporting Information). The device with improved thermal management generated improved Seebeck output by 21% and 16% at 10 and 60 °C respectively (Figure 2e,i). The experimentally measured Seebeck performance of TEDs is analytically supported by finite element analysis (FEA). As shown in Figure S6d,e (Supporting Information), the thermoelectric simulation confirms that employing LM-epoxy as a thermal interface improves peak voltage output compared to control epoxy. FEA and experimental results both indicate voltage output peaking quickly, followed by a gradual descent as heat transfers through the device. The simulated voltages show similar trends with experimental results, computationally validating the Seebeck measurement (Section S1, Supporting Information).

Power output was characterized with an external varied resistor acting as the load. Power output is shown in Figure S5c (Supporting Information) with power (P) being determined by $P = \frac{V^2}{R_{ext}}$ where V is the voltage across the external load resistor and R_{ext} is the external resistance. Power peaked at 1.89, 7.81, and 17.27 mW at a 20, 40, 60 °C ΔT along with a 0.154, 0.635, and 1.404 mWcm^{-2} power density respectively.

**ADVANCED
SCIENCE NEWS**

www.advancedsciencenews.com

**ADVANCED
FUNCTIONAL
MATERIALS**

www.afm-journal.de

TEDs with the addition of the LM-epoxy TIM exhibited improved Peltier cooling performance and decreased Peltier heating performance over the control epoxy device, with peak cooling ΔT of -8.4 ± 1.2 °C @ 0.50 A at 44.3 s for HA-LD + LM-epoxy versus -6.4 ± 0.3 @ 0.50 A at 41.3 s for HA-LD + Control Epoxy (Figure 2f,k; Figures S7d and S12a,b, Supporting Information). Thermal imaging has shown improved thermal performance in distributing heat over the area of the Peltier cooler compared with the control (Figure S13, Supporting Information).

HA-LD + LM-epoxy mechanical performance was similar to that without LM-epoxy (Figure 2g,h), with $P_{cr} = 1.70$ N and flexural rigidity of 9.11×10^{-5} Nm^2. No mechanical or electrical failure occurred (Figure 3a,b). Similar results were recorded for a high-loading cycle test that was conducted for 380 cycles at 0 % and 20 % strain, again with no mechanical or electrical failure at the end of this test (Figure 3c,d). A 10-cycle uniaxial strain test at 30 % was conducted with a peak relative resistance increase of ≈ 0.20 (Figure 3e,f).

LM-epoxy improved Seebeck harvesting, Peltier cooling, and mechanical robustness. A final HA-HD device with LM-epoxy was fabricated. The power output of a HA-HD + LM-epoxy harvester at 20, 40, and 60 °C with an external resistor as a load was characterized (Figure 2l). Power outputs are 4.95 (0.402 mWcm^{-2}), 17.79 (1.647 mWcm^{-2}), and 35.85 mW (3.318 mWcm^{-2}) respectively. This was a large improvement in power density over HA-LD harvesters without LM-epoxy (Figure 2m). Comparisons of electrical and mechanical performance with other TEG research can be found in Table S1 (Supporting Information).

2.3. On-Body Wearable Integration

To determine the real-world compatibility of the proposed TEGsense design, we characterized the device with user studies in both a laboratory setting and an outdoor environment. Importantly, our data suggests that various environmental (windspeed, temperature) and physiological conditions (correlated with heart rate, as measured) influence TEG voltage output. We designed our study to probe at the general influence of bio-mechanical movement, physical exertion, and device location on the user's body to better understand the average and peak power outputs. Specifically, we ran tests with TEGs integrated into wrist-worn and chest-worn garments while sitting, and compared to walking and running on a treadmill. Finally, we asked our user to walk outdoors at a normal pace while wearing TEGsense, an 8 TEG array along with a circuit board for processing and Bluetooth data transmission. We should note that, while these studies involved heart rate tracking, they did not directly measure metabolic energy consumption or the influence of the worn TEG device on metabolic cost.

To test the influence of bio-mechanical and physiological factors, we conducted trials on a treadmill with TEGs integrated into the subject's clothing. In particular, the influence of human motion on increasing the convective cooling rate on the outside of the TEG, the role of exercise on conductive heating from the body onto the inside of the TEG, and the influence of TEG body location on Seebeck performance were all explored (**Figure 4a,b**). To accomplish this, an experimental setup was designed with HA-LD + LM-epoxy TEGs mounted on the wrist and chest embedded with a thermocouple temperature sensor on each side and integrated into compression clothing. Heart rate was also monitored during these tests (see Experimental Section). Wrist and chest placement were chosen due to their differences in relative motion during walking and running, along with these placements corresponding to the locations of wearable health monitoring systems.

2.3.1. Sit-Walk Test Results

We investigated Seebeck performance during sitting and walking tests with TEGs mounted on the wrist and chest. The influence of increased convective cooling from bio-mechanical movement on the wrist-worn device was clear. For the wrist sit-walk test, movement across the device's outside face during walking lowered the surface temperature leading to a ≈ 20 % increase in relative voltage (Figures S14a and S15a, Supporting Information). For the chest-worn device, temperature stayed consistent for both sitting and walking (Figures S14b and S15b, Supporting Information) from no additional airflow across the device, as chest movement was limited during these treadmill-based tests.

2.3.2. Sit-Run Test Results

Data for the sit-run chest and wrist test are given in Figure 4c,d. Both cooling from bio-mechanical motion and heating from exercise played a major role in TEG Seebeck output with a > 1.0 relative voltage change for the wrist-worn device and 0.8 relative voltage change for the chest worn device (Figure S15c,d, Supporting Information). Sweat was also found on the inside of the device after testing which may help to decrease thermal resistance.

While these initial tests helped to inform the influence of bio-mechanical motion and exertion on TEG Seebeck performance, no sit-run tests reached a steady state for voltage or temperature values. A longer test was conducted to determine if the Seebeck improvement would plateau. Results are shown in Figure 4e and Figure S16 (Supporting Information). When comparing voltage, temperature differential, and heart rate, one can see that these all began to plateau ≈ 1000 s indicating a steady state and stable voltage output. Based on these wearable tests, we can predict large (> 2X) consistent Seebeck improvement during exertion. To investigate a general trend of the harvested voltage, FEA for the sit–run test is conducted. While the inside and outside temperatures are determined as boundary conditions, the simulated voltage agreeably matches with the experimental output. It also demonstrates that the estimation on wearable TEG is possible even with the complicated working conditions, including both sedentary and running subject as a heat source. See Section S3 (Supporting Information) for expanded discussion on wearable testing. For integration into a fully functional wearable devices, the wrist-worn orientation was selected as it exhibits superior Seebeck performance during testing.

2.3.3. TEGsense Wearable Performance

To address the lifespan and data transmission issues associated with battery powered wearables, we introduce a large thermoelectric generator array (TEGsense) and demonstrate battery free
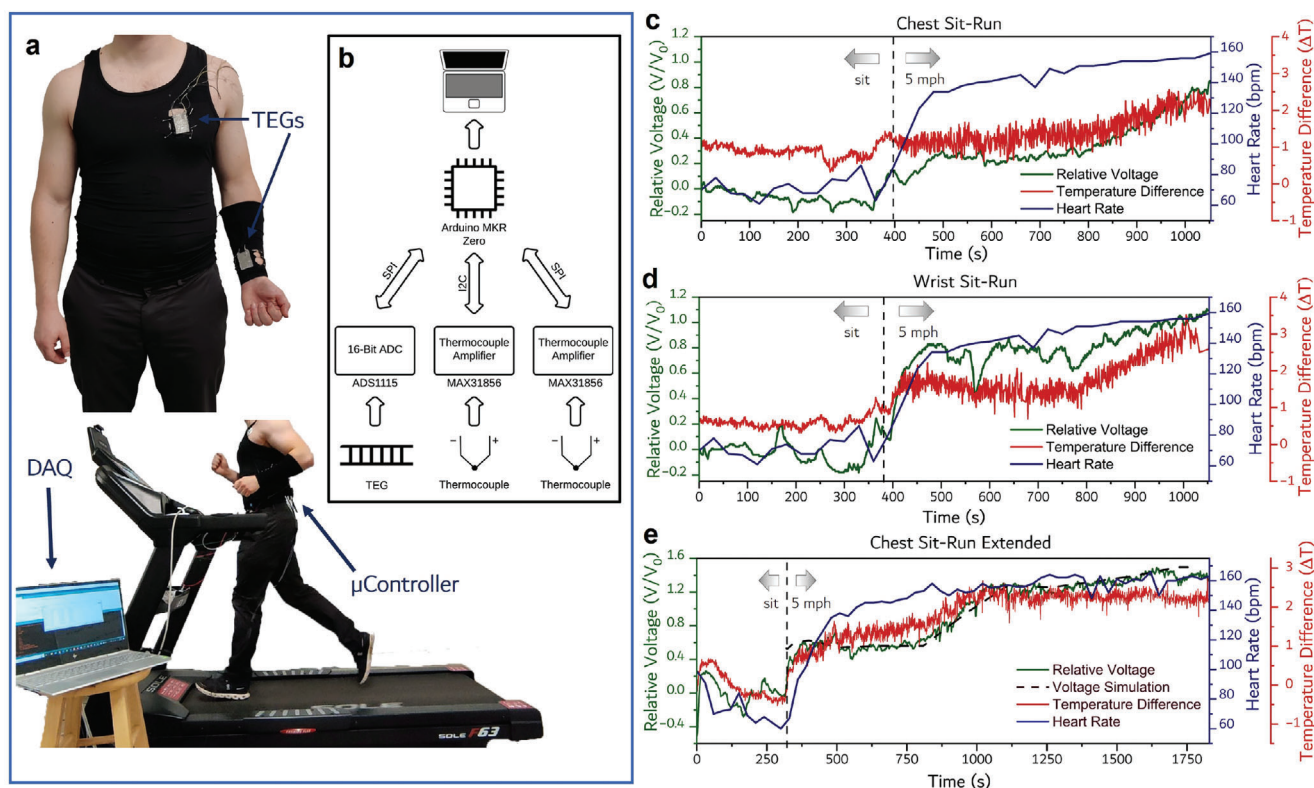
**ADVANCED
SCIENCE NEWS**

www.advancedsciencenews.com

**ADVANCED
FUNCTIONAL
MATERIALS**

www.afm-journal.de

Figure 4. Wearable Testing. a) Top: image of experimental set-up for TED placement on the wrist and chest. Bottom: image taken during a run test at 5 mph highlighting placement of one of the µcontrollers. b) Block diagram of circuitry used for data collection. c–e) Results of wearable treadmill testing for wrist and chest worn devices during sit-run testing.

medical sensing and wireless data transmission. TEGsense consists of 8 HA-HD+LM-epoxy TEGs integrated into a forearm sleeve connected to a capacitor array and custom low-power photonic PPG board (**Figure** 5a,b). As shown during wearable testing, the wrist location was chosen as limb movement leads to a significant increase in convective cooling leading to a Seebeck energy harvesting boost. Power generated from the TEG array is initially boosted to 4.1 V using a low-power boost converter to charge a 10.8 mF cap array. Once charged, the TEGsense board records the photoplethysmogram (PPG) wave-form. This data is then sent over Bluetooth low energy (BLE) with the board reentering a hibernation state. This repeats indefinitely while a temperature differential is held across the device. Further details can be found in the Experimental Section.

Results of the TEG array's charge rate is show in Figure 5c. TEGsense is run for five cycles with alternating standing and walking conditions on a cold day (6.6 °C) to understand the approximate charge times need to run the TEGsense board. TEGsense output voltage and capacitor charge voltage are shown indicating the short charge times for TEGsense board operation. During charging cycles, the wearer walks and charges the capacitor array for ≈3 min. During cycles 4 and 5, the limb began to get cold due to outdoor exposure, leading to an increase in charge time, highlighting the influence of physiological conditions on performance. Because of the variability in charging time, complete discharging of the capacitors to power the circuit board was timed to occur every 6 min. In general, this resulted in time periods of ≈2–3 min. where the user was either walking or standing and no longer charging the capacitors. Following this validation of the device power management, we performed a separate set of experiments on another day in 2 °C weather in which TEGsense was used to operate a photonic PPG-sensing wearable. Capacitors were charged up during ≈4 min. of walking and then discharged to operate a circuit with a photonic pulse oximetry chip for PPG data collection, microcontroller for signal processing, and Bluetooth transmitter for wireless output of PPG waveforms to an external receiver. PPG waveforms were collected and recorded for both Red and IR (Figure 5d). The corresponding voltage data with the 4 min. charge time can be found in Figure S17 (Supporting Information). See Video S2 (Supporting Information) for a demonstration of both the indoor and outdoor operations.

3. Conclusion

In this work, we introduce a framework for creating soft, flexible, and stretchable thermoelectric generators for powering body-mounted electronics. This includes the development of TEGsense, an integrated health monitoring wearable that converts energy from body heat into electricity used for battery-free operation of a photonic sensing device. Using this framework, we introduce new material architectures and design approaches for fabricating high-performance bendable and stretchable TEGs, explore the influence of biomechanical movement on device performance, and integrate these TEGs into a PPG monitoring
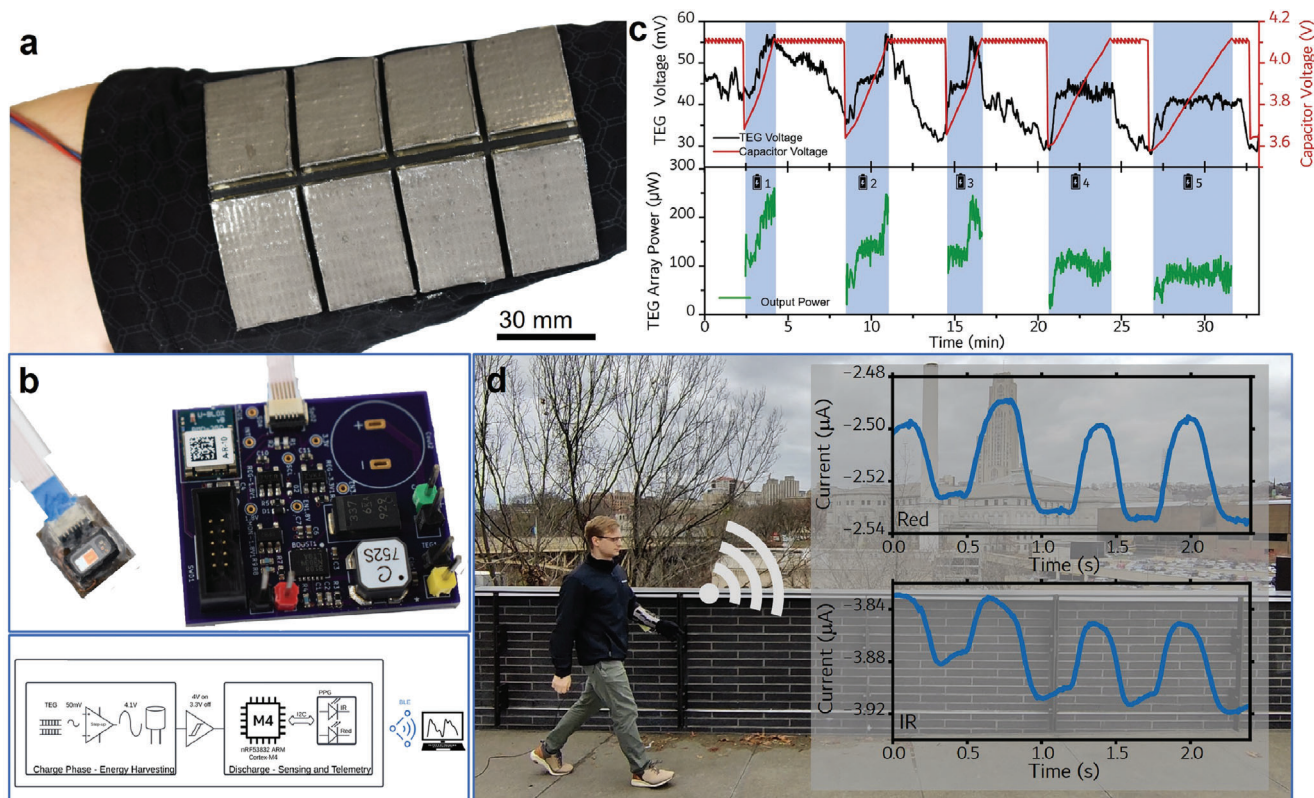
**ADVANCED
SCIENCE NEWS**

www.advancedsciencenews.com

**ADVANCED
FUNCTIONAL
MATERIALS**

www.afm-journal.de

Figure 5. TEGsense implementation and testing. a) Image of eight HA-HD+LM-epoxy TEGs intergrated into TEGsense array. b) Top: Image of TEGsense board integrated with processor, BLE, boost converter, and photonic chip. Bottom: TEGsense board block diagram. The thermoelectric generators use the temperature gradient between the body and the environment to generate a low voltage potential ($\approx$50 mV), which is boosted by a step-up voltage converter to charge a capacitor bank to 4.1 V. A hysteretic switch powers on the microcontroller and sensor when the capacitors rise above 4 V. Once on, the microcontroller collects red and infrared light reflection measurements from a photoplethysmograph sensor. This waveform is telemetered to an external laptop over Bluetooth. Finally, when voltage drops below 3.3 V, the switch disconnects power to the microcontroller and sensor. Once on, the microcontroller collects red and infrared light reflection measurements from a photoplethysmograph sensor. This waveform is telemetered to an external laptop over Bluetooth. c) Voltage versus time data for both the TEGsense array voltage into the step-up converter, and the boosted voltage from the step-up converter into the 10.8 mF capacitor bank. The bottom concurrent plot shows the power output during the blue-shaded charging periods. d) Red and IR PPG waveform data being transmitted over BLE after energy harvesting and data collection during testing.

wearable. To enable development of these TEGs, we incorporated interconnects made of LM-Ag-SIS inks, enabling low internal electrical resistance and high semiconductor densities.[43] Additionally, a thermally conductive (2.90 ± 0.02 Wm^{-1} K^{-1}) and mechanically compliant LM-epoxy composite was used as an interface material, and 3D printing was utilized to design hollow internal structures to decrease device stiffness.

A peak power output of 35.85 mW (3.318 mWcm^{-2}) is achieved at 60 °$C \Delta T$. Mechanically, these harvesters were found to operate with no mechanical or electrical failure at 30 % uniaxial strain, and they showed no electrical or mechanical performance degradation after 380 cycles at 20 % compression. As a Peltier cooler, a maximum change in temperature of $\Delta T = -13.0 \pm 0.6$ °C was generated at 0.75 A. Bio-mechanical testing with the wearable TEGs was performed to better understand the relationship between physical exertion, bio-mechanical movement, and TEG placement on device Seebeck harvesting. These tests concluded that wrist-worn TEGs experience large improvements (2X) in voltage output during running (5.0 mph).

Current limitations of this work suggest a few main areas of improvement. First, for flexible TEGs to gain adoption in the commercial space, these generators need to be produced using automated manufacturing methods compatible with production-grade manufacturing lines. Future efforts to address this can include using pick-and-place machines to improve precision and decrease manufacturing time. Second, to increase power output, the internal resistance of the devices must be further reduced. In particular, new approaches are needed to mitigate the semiconductor-interconnect contact resistance. This will require improvements in surface coatings of the semiconductors, along with improving the conductivity of LM-based inks. Formulations of EGaIn with a high percentage oxide (OGaIn) are potentially one direction to have scalable and repeatable fabrication, while simultaneously improving electrical conductivity to more closely approach the bulk conductivity of LM.[47] Such an improvement could lead to greater performance in ambient indoor conditions, since decreased internal resistance would allow for improved impedance matching with boost converters. Separately, coupling with other wearable energy harvesting modalities such a triboelectric or piezoelectric harvesting is another avenue for improved performance. Another consideration that needs to be better explored and addressed in future work is the impact

**ADVANCED
SCIENCE NEWS**

www.advancedsciencenews.com

**ADVANCED
FUNCTIONAL
MATERIALS**

www.afm-journal.de

of liquid metal wearables on human skin over a long period of time. With repeated use on the body, the LM-epoxy layer has a tendency to rub off onto the skin. Although previous work suggests that LM-polymer composites are not cytotoxic,[48] further study is required. Additional work will need to be conducted to better understand LM's introduction into wearables. Waterproofing of these energy harvesters will also need to be explored for underwater applications along with their use in rainy or snowy environments.[39] Lastly, while most components of TEGsense were made soft and stretchable, the semiconductors are still rigid, leading to stress concentrations on the semiconductor-elastomer interface. To address this, progress depends on further miniaturization of the thermoelectric semiconductors or the use of semiconductor materials that are intrinsically soft and deformable. One particular direction would be to focus on 3D printed thermoelectric semiconductors prepared in a slurry and direct-ink-write printed to directly replace their rigid counterparts.[49]

4. Experimental Section

Elastomeric Resin Composition: The center layers and stencils were 3D printed using a material composed of 49.02 wt.% of epoxy aliphatic acrylate (EAA, Ebecryl 113, Allnex USA), 49.02 wt.% of aliphatic urethane acrylate (AUD, Ebecryl 8413, Allnex, USA), and 1.96 wt.% TPO (diphenyl(2,4,6-trimethylbenzoyl)phosphine oxide, Genocure TPO, RAHN USA Corp.) as the photoinitiator. TPO was dissolved in elastomeric monomers in a hot water bath at 86 °C.

3D Printing: A DLP 3D printer (PicoHD@27, Asiga) was used for all printing. Printing occurred at 40 °C, with each layer irradiated for 0.5 s, with a layer thickness of 100 μm. Once printed, the structures were sonicated in isopropyl alcohol (IPA) for 3 min. to clean off uncured resin. Detailed printing parameters can be found in Table S2 (Supporting Information).

Thermoelectric Device Fabrication: Images of the fabrication process can be found in Figure S1 (Supporting Information). The center layer of the TEGs was first printed using DLP printing (Figure S1–i, Supporting Information). The dimensions for the active areas of the TED's various configurations were: 42.7 × 22.6 × 1.6 mm, 200 semiconductors, and a fill density of 40.6 % for LA-HD, 41 × 30 × 4 mm, 140 semiconductors, and a fill density of 22.3 % for HA-LD, 38.9 × 27.7 × 4 mm, 216 semiconductors, and a fill density of 39.2 % for HA-HD (Table S3, Supporting Information). Next, p and n-type semiconductors were placed into the printed holes in P-N π configuration (Figure S1ii, Supporting Information). Depending on the configuration, the semiconductors used were 1.4 × 1.4 × 1.6 mm 99.99 % purity Bi_2Te_3 semiconductors (Wuhan Xinrong New Materials Co., Ltd.) and 1.4 × 1.4 × 4 mm Bi_2Te_3 semiconductors (Ningbo Sen Ao electronic Technology Co., Ltd). A 1 mm thick DLP-printed soft stencil was then placed over the device, forming a seal between the device and stencil (Figure S1–iii, Supporting Information). A light layer of EGaIn was then airbrushed onto the openings of the stencil to mitigate contact resistance (Figure S1–iv, Supporting Information).

Next, bi-phasic LM-Ag-SIS inks were formulated. Styrene-isoprene block copolymers (SIS, Sigma–Aldrich) were dissolved in toluene (1.5:8.5) at 100 °C for 1 h. Once a clear and homogeneous solution was obtained, 1.54 Ag flakes (SF 94, Ames Goldsmith corp.) were added to 1 g SIS solution, then hand mixed for 30 s to disperse the micro-sized flakes. Then, 2.7 g EGaIn was added and hand mixed. This solution was then planetary mixed for 3 min. at 2000 RPM. The ink was then loaded into a syringe for controlled injection into each of the interconnect wells created by the soft stencil layer (Figure S1v, Supporting Information). To mitigate warping of the soft stencil and toluene evaporation, this process was done on a cold surface. The stencils were then removed, leaving the semiconductors (Figure S1vi, Supporting Information). The trace width separation between interconnects was 700 μm. To evaporate the toluene, the device was placed on a hot plate for 1 h at 60 °C. Next, a planetary mixer was

used to make a 65 vol% LM dispersion of LM in epoxy, and deposited a 700 μm layer over the conductive interconnects using a thin film applicator (Figure S1vii, Supporting Information). The LM-epoxy was left to settle overnight, followed by 1 h curing at 60 °C and 1 h curing at 120 °C. The control specimens were fabricated using an identical procedure, except the final LM-epoxy coating was substituted with neat epoxy. For devices without a coating (either LM-epoxy or neat epoxy), the UV curable ink used in the 3D printing process was coated onto the surface with a brush and then cured with λ = 365 nm UV irradiation at 5 W for 12 min. (Warson R838). This process was then repeated on the back side (Figure S1viii, Supporting Information). Finally, copper tape or braided wire was affixed to form electrical leads.

Thermoelectric Testing: To measure the thermoelectric performance of the thermoelectric devices, the devices were placed on a hot plate with a computer heat sink applied to the opposite side (to improve the temperature differential), and simultaneously recorded the voltages and temperatures. Each device configuration was tested three times. Peak voltage values were recorded before the temperature differential degraded due to heat transfer. Power output was recorded by measuring voltage in parallel with an external load resistor, where $P = \frac{V^2}{R_{ext}}$. The peak voltage was again recorded. Peltier heating and cooling occurred when a current was applied across the thermoelectric device.[50] For Peltier measurements, a representative spot temperature measurement was taken for three cycles at each current using a thermal camera (FLIR A35, Teledyne FlIR LLC). All tests were conducted at room temperature.

Mechanical and Thermal Testing: For mechanical testing, the length of the non-active section of the TEGs was extended, to allow the devices to be mounted into a universal materials tester (Instron 5969, with 50 N load cell). Euler's critical load is defined as $P_{cr} = \frac{2\pi EI}{K^2L^2}$ where $L = 46$ mm is the length of the beam and $K = 0.5$ is the column effective length factor. For peel tests, a sample of the 3D printed acrylate with active dimensions of 23.5 × 35 × 0.7 mm coated with 0.5 mm of 60 vol % LM-epoxy. This was then placed in the Instron and subjected to a θ = 180° T-peel loading condition. Work of adhesion (W) was defined as $W = (1 - \cos\theta)PL$ where P is the force of peel of 1.15 N and L is the width of the sample at 23.5 mm.[51] For thermal testing, a thermal interface material analyzer was used (TIMA5, Nanotest) to record the thermal resistance and thermal conductivity of uncured 65 vol% LM-epoxy at various thicknesses from 500 − 1000 μm. The reported values at each bondline thickness were an average of 40 data points.

Finite Element Analysis Simulations: The time-dependent energy harvesting of the TEG devices was simulated using FEA software COMSOL Multiphysics. The considered physics was heat transfer, electric currents, and thermoelectric effects. The representative volume element method was applied, to improve computational efficiency and scalability. To match the physical experiments, the simulation time-step was set to 0.855 s. The input boundary conditions were the temperatures on the TEG's bottom thermal interface, and the output was the thermoelectrically harvested voltages. For simulating the different types of LA-HD voltage output with respect to time, a 5 cm tall aluminum block was placed on top of the TEGs, matching the experimental condition, and the convective heat transfer coefficient of air was set to 10 Wm^{-2} K^{-1}. However, for simulating the wearable test, a root mean squared air velocity of 0.3 ms^{-1} was used, corresponding to a slow walking pace. See Table S4 (Supporting Information) for a more complete listing of the parameters used in the simulations.

Wearable Testing: To test the performance of TEG devices when worn by a user who was operating a treadmill, the participant wore one HA-LD+LM-epoxy TED on the inside of their left wrist and another on the left side of their chest. A K-type thermocouple was integrated on each side of each HA-LD+LM-epoxy TED, and the final TEG+thermocouple pair was integrated into a compression garment. Each TEG was connected to an Arduino MKR Zero board that read voltage data from a ADS1115 16-bit ADC (Adafruit, LLC), read temperature data from two thermocouple amplifier MAX31856 boards (Adafruit, LLC), and finally logged all the data to a micro SD card. Simultaneously, the user's heart rate was measured using an ECG (Zoll, Inc.). Two sets of initial tests were conducted: sitting (≈375 s) followed by walking (2 mph for ≈375 s), and sitting (≈375 s)

ADVANCED
SCIENCE NEWS

www.advancedsciencenews.com

ADVANCED
FUNCTIONAL
MATERIALS

www.afm-journal.de

followed by running (5 mph for ≈675 s). To reduce signal noise, the temperature data was pre-processed with manual outlier rejection followed by a low-pass filter with a cutoff frequency of 0.032 Hz when needed. Finally, a third test was conducted to provide more insight into the steady-state settling time: sitting (≈320 s) followed by running (5 mph for ≈1500 s).

TEGsense Board Design: A fully TEG-powered custom printed circuit board (PCB) was developed with integrated power management, sensing, and control hardware. In contrast to the PC-powered Arduino configuration just described for TED characterization, this circuit was designed to leverage those experiments and enable a fully body-heat powered device. The TEGsense board (see https://github.com/TEGSense and Figure S18, Supporting Information) used a ultra-low voltage step-up converter (Linear Technology LTC3108) to boost a low voltage TEG input (≈50 mV) and charged a 10.8 mF capacitor bank to 4.1 V. To minimize energy loss and achieve sufficient surge current to power on the microcontroller, low equivalent series resistance (ESR) aluminum polymer capacitors (Elite UGS1C272MP51020F5RU, 10 mΩ) were used. A hysteretic voltage monitor (Microchip MIC2779) was used to enable the 1.8 and 3.3 V regulators once the capacitor bank reached 4 V. If the charge fell below 3.3 V, the monitor disabled the downstream regulators, thus turning off the microcontroller. To capture sensor data over an inter-integrated circuit (I2C) and then relay that data to an external PC via BLE, the circuit used a module (u-blox BMD-350) that had an integrated chip antenna and a Bluetooth Low Energy (BLE) enabled microcontroller (Nordic Semiconductor nRF52832). A finger-worn photoplethysmograph (PPG) sensor (Maxim Integrated MAX30101) sensed infrared (IR) and red light reflected by skin tissue at 100 Hz for a period of 3 s per sampling event. The first sampling event occurred when the microcontroller was turned on (i.e., after the capacitor voltage reached 4 V). Subsequent measurements were recorded at 6 min. intervals, as long as the minimum capacitor voltage (3.3 V) was maintained. The red and IR PPG waveforms were received by an external PC for subsequent analysis.

TEGsense Demonstration: TEGsense was fabricated in the same way as previously described for HA-HD+LM-epoxy TEGs. TEGsense comprised eight HA-HD+LM-epoxy TEGs wired in parallel into an array with overall dimensions of 12.7 × 9.5 cm. This was then integrated into an elastic compression sleeve and worn on the forearm. A hole was cut into the compression sleeve to allow for the TEG to be integrated and mounted directly on the skin when worn. To achieve the highest efficiency, TEGsense's electrical resistance needed to be in the range of $2 - 10\,\Omega$ for impedance matching with the booster converter. Considering each TEG had an internal resistance of $\sim 8 - 10\,\Omega$, a series configuration leaves a large impedance mismatch. To circumvent this, TEGsense TEGs were configured in a parallel configuration decreasing overall impedance within the range. Low effective series resistance (ESR) of the capacitors was needed to decrease capacitor charge time. To accomplish this a parallel array of four 2.7 mF aluminum polymer capacitors was selected as opposed to a higher ESR supercapacitor.

Supporting Information

Supporting Information is available from the Wiley Online Library or from the author.

Acknowledgements

Conflict of Interest

The authors declare no conflict of interest.

Data Availability Statement

The data that support the findings of this study are available in the supplementary material of this article.

Keywords

[1] M. Zadan, C. Chiew, C. Majidi, M. H. Malakooti, *Multifunct. Mater.* **2021**, *4*, 012001.
[2] V. Nair, A. N. Dalrymple, Z. Yu, G. Balakrishnan, C. J. Bettinger, D. J. Weber, K. Yang, J. T. Robinson, *Science* **2023**, *382*, eabn4732.
[3] R. Riemer, A. Shapiro, *J. Neuroeng. Rehab.* **2011**, *8*, 1.
[4] A. S. Khan, F. U. Khan, *Int. J. Energy Res.* **2022**, *46*, 2277.
[5] Y.-W. Chong, W. Ismail, K. Ko, C.-Y. Lee, *IEEE Sens. J.* **2019**, *19*, 9047.
[6] A. R. M. Siddique, S. Mahmud, B. Van Heyst, *Renewable Sustainable Energy Rev.* **2017**, *73*, 730.
[7] M. Dargusch, W.-D. Liu, Z.-G. Chen, *Adv. Sci.* **2020**, *7*, 2001362.
[8] X.-L. Shi, J. Zou, Z.-G. Chen, *Chem. Rev.* **2020**, *120*, 7399.
[9] M. Sattar, W.-H. Yeo, *Materials* **2022**, *15*, 4315.
[10] Y. Yang, H. Hu, Z. Chen, Z. Wang, L. Jiang, G. Lu, X. Li, R. Chen, J. Jin, H. Kang, H. Chen, S. Lin, S. Xiao, H. Zhao, R.Xiong, J. Shi, Q. Zhou, S. Xu, S. Xu, Y. Chen, Y. Chen, *Nano Lett.* **2020**, *20*, 4445.
[11] S. Hong, Y. Gu, J. K. Seo, J. Wang, P. Liu, Y. S. Meng, S. Xu, R. Chen, *Sci. Adv.* **2019**, *5*, eaaw0536.
[12] S. H. Jeong, F. J. Cruz, S. Chen, L. Gravier, J. Liu, Z. Wu, K. Hjort, S.-L. Zhang, Z.-B. Zhang, *ACS Appl. Mater. Interfaces* **2017**, *9*, 15791.
[13] M. Zadan, D. K. Patel, A. P. Sabelhaus, J. Liao, A. Wertz, L. Yao, C. Majidi, *Adv. Mater.* **2022**, *34*, 2200857.
[14] F. Suarez, D. P. Parekh, C. Ladd, D. Vashaee, M. D. Dickey, M. C. Öztürk, *Appl. Energy* **2017**, *202*, 736.
[15] H. You, Z. Li, Y. Shao, X. Yuan, W. Liu, H. Tang, Q. Zhang, Y. Yan, X. Tang, *Appl. Therm. Eng.* **2022**, *202*, 117818.
[16] S. J. Kim, H. E. Lee, H. Choi, Y. Kim, J. H. We, J. S. Shin, K. J. Lee, B. J. Cho, *ACS Nano* **2016**, *10*, 10851.
[17] Z. An, Q. Fu, J. Lv, T. Zhou, Y. Wu, Y. Lu, G. Liu, Z. Shi, X. li, F. Zhang, Q. Liu, *Adv. Funct. Mater.* **2023**, *33*, 2303361.
[18] V. Padmanabhan Ramesh, Y. Sargolzaeiaval, T. Neumann, V. Misra, D. Vashaee, M. D. Dickey, M. C. Ozturk, *npj Flexible Electron.* **2021**, *5*, 5.
[19] Y. Han, L.-E. Simonsen, M. H. Malakooti, *Adv. Energy Mater.* **2022**, *12*, 2201413.
[20] T. Pan, M. Pharr, Y. Ma, R. Ning, Z. Yan, R. Xu, X. Feng, Y. Huang, J. A. Rogers, *Adv. Funct. Mater.* **2017**, *27*, 1702589.
[21] F. Bossuyt, T. Vervust, J. Vanfleteren, *IEEE Trans. Compon. Packag. Manuf. Technol.* **2013**, *3*, 229.

**ADVANCED
SCIENCE NEWS**

www.advancedsciencenews.com

**ADVANCED
FUNCTIONAL
MATERIALS**

www.afm-journal.de

[22] Z. J. Farrell, C. Tabor, *Langmuir* **2018**, *34*, 234.

[23] C. J. Thrasher, Z. J. Farrell, N. J. Morris, C. L. Willey, C. E. Tabor, *Adv. Mater.* **2019**, *31*, 1903864.

[24] M. Zadan, M. H. Malakooti, C. Majidi, *ACS Appl. Mater. Interfaces* **2020**, *12*, 17921.

[25] J. Lee, H. Sul, Y. Jung, H. Kim, S. Han, J. Choi, J. Shin, D. Kim, J. Jung, S. Hong, et al., *Adv. Funct. Mater.* **2020**, *30*, 2003328.

[26] P. Won, C. S. Valentine, M. Zadan, C. Pan, M. Vinciguerra, D. K. Patel, S. H. Ko, L. M. Walker, C. Majidi, *ACS Appl. Mater. Interfaces* **2022**, *14*, 55028.

[27] R. Herbert, P. Mocny, Y. Zhao, T.-C. Lin, J. Zhang, M. Vinciguerra, S. Surprenant, W. Y. D. Chan, S. Kumar, M. R. Bockstaller, K. Matyjaszewski, C. Majidi, *Adv. Funct. Mater.* **2023**, https://doi.org/10.1002/adfm.202309725.

[28] Y. Liu, S. Hou, X. Wang, L. Yin, Z. Wu, X. Wang, J. Mao, J. Sui, X. Liu, Q. Zhang, Z.Liu, F. Cao, *Small* **2022**, *18*, 2106875.

[29] G. Lee, C. S. Kim, S. Kim, Y. J. Kim, H. Choi, B. J. Cho, *Energy* **2019**, *179*, 12.

[30] Y. Sargolzaeiaval, V. P. Ramesh, T. V. Neumann, V. Misra, D. Vashaee, M. D. Dickey, M. C. Öztürk, *Appl. Energy* **2020**, *262*, 114370.

[31] B. Lee, H. Cho, K. T. Park, J.-S. Kim, M. Park, H. Kim, Y. Hong, S. Chung, *Nat. Commun.* **2020**, *11*, 1.

[32] H. Wei, J. Zhang, Y. Han, D. Xu, *Appl. Energy* **2022**, *326*, 119941.

[33] J. Yuan, R. Zhu, *Appl. Energy* **2020**, *271*, 115250.

[34] C. S. Kim, H. M. Yang, J. Lee, G. S. Lee, H. Choi, Y. J. Kim, S. H. Lim, S. H. Cho, B. J. Cho, *ACS Energy Lett.* **2018**, *3*, 501.

[35] Y. Wang, Y. Shi, D. Mei, Z. Chen, *Appl. Energy* **2018**, *215*, 690.

[36] J. Park, G. Bhat, A. Nk, C. S. Geyik, U. Y. Ogras, H. G. Lee, *Sensors* **2020**, *20*, 764.

[37] A. Nozariasbmarz, R. A. Kishore, B. Poudel, U. Saparamadu, W. Li, R. Cruz, S. Priya, *ACS Appl. Mater. Interfaces* **2019**, *11*, 40107.

[38] Y. Sargolzaeiaval, V. P. Ramesh, M. C. Ozturk, *Appl. Energy* **2022**, *324*, 119738.

[39] Y. Jung, J. Choi, Y. Yoon, H. Park, J. Lee, S. H. Ko, *Nano Energy* **2022**, *95*, 107002.

[40] D. K. Patel, A. H. Sakhaei, M. Layani, B. Zhang, Q. Ge, S. Magdassi, *Adv. Mater.* **2017**, *29*, 1606000.

[41] Z. J. Patterson, D. K. Patel, S. Bergbreiter, L. Yao, C. Majidi, *Soft Robotics* **2023**, *10*, 292.

[42] W. Zu, Y. Ohm, M. R. Carneiro, M. Vinciguerra, M. Tavakoli, C. Majidi, *Adv. Mater. Technologies* **2022**, *7*, 2200534.

[43] P. A. Lopes, D. F. Fernandes, A. F. Silva, D. G. Marques, A. T. de Almeida, C. Majidi, M. Tavakoli, *ACS Appl. Mater. Interfaces* **2021**, *13*, 14552.

[44] S. Yu, M. Kaviany, *J. Chem. Phys.* **2014**, *140*, 6.

[45] M. D. Bartlett, N. Kazem, M. J. Powell-Palm, X. Huang, W. Sun, J. A. Malen, C. Majidi, *Proc. Natl. Acad. Sci.* **2017**, *114*, 2143.

[46] N. Kazem, T. Hellebrekers, C. Majidi, *Adv. Mater.* **2017**, *29*, 1605985.

[47] W. Kong, N. U. H. Shah, T. V. Neumann, M. H. Vong, P. Kotagama, M. D. Dickey, R. Y. Wang, K. Rykaczewski, *Soft Matter* **2020**, *16*, 5801.

[48] P. Won, S. Coyle, S. H. Ko, D. Quinn, K. J. Hsia, P. LeDuc, C. Majidi, *Adv. Healthcare Mater.* **2023**, *12*, 2202430.

[49] D. Zhang, W. Y. S. Lim, S. S. F. Duran, X. J. Loh, A. Suwardi, *ACS Energy Lett.* **2022**, *7*, 720.

[50] C. Choi, Y. Ma, X. Li, S. Chatterjee, S. Sequeira, R. F. Friesen, J. R. Felts, M. C. Hipwell, *Sci. Rob.* **2022**, *7*, eabl4543.

[51] K. Kendall, *J. Phys. D: Appl. Phys.* **1971**, *4*, 1186.

[52] M. R. Vinciguerra, D. K. Patel, W. Zu, M. Tavakoli, C. Majidi, L. Yao, *ACS Appl. Mater. Interfaces* **2023**, *15*, 24777.

[53] M. H. Malakooti, N. Kazem, J. Yan, C. F. Pan, E. J. Markvicka, K. Matyjaszewski, C. Majidi, *Adv. Funct. Mater.* **2019**, *29*, 1906098.

2404861 (12 of 12)